Received: 10 June 2022 | Revised: 1 August 2022 | Accepted: 18 August 2022

DOI: 10.1002/er.8675

SPECIAL ISSUE RESEARCH ARTICLE

INTERNATIONAL JOURNAL OF ENERGY RESEARCH WILEY

A novel green technology: Reducing carbon dioxide and eliminating methane from the atmosphere

Tingzhen Ming[1,2] | **Hanbing Xiong**[1] | **Tianhao Shi**[1] | **Yongjia Wu**[1] | **Caixia Wang**[1] | **Yuangao Wen**[1] | **Wei Li**[3] | **Renaud de Richter**[4] | **Nan Zhou**[5]

[1]School of Civil Engineering and Architecture, Wuhan University of Technology, Wuhan, China

[2]School of Architectural Engineering, Huanggang Normal University, Huanggang, China

[3]Institute for Materials and Processes, School of Engineering, The University of Edinburgh, Edinburgh, UK

[4]Tour-Solaire. Fr, 8 Impasse des Papillons, Montpellier, France

[5]Energy Technologies Area, Lawrence Berkeley National Laboratory, Berkeley, California, USA

Correspondence
Yongjia Wu, School of Civil Engineering and Architecture, Wuhan University of Technology, Wuhan 430070, China.
Email: yjwu2019@whut.edu.cn

Yuangao Wen, School of Civil Engineering and Architecture, Wuhan University of Technology, Wuhan 430070, China.
Email: wenyg2000@128.com

Funding information
European Commission H2020 Marie Curie Research and Innovation Staff Exchange (RISE), Grant/Award Number: 871998; National Key Research and Development Plan (special Project of Inter-governmental National Scientific and Technological Innovation Cooperation), Grant/Award Number: 2019YFE0197500

Summary

The greenhouse effect is exacerbated as greenhouse gas concentrations rise. Capturing and degrading methane in the atmosphere can effectively slow the trend of global temperature rise. The solar chimney power plant integrated with photocatalytic reactor (SCPP-PCR) is a promising concept for both clean electricity generation and large-scale atmospheric methane removal. In this paper, this concept was for the first time quantitatively verified by integrating a photocatalytic reactor in the collector of SCPP to realize the above two targets. A systematic numerical model was proposed to evaluate the performance of degradation of methane and the electricity generation of the SCPP-PCR. The results revealed that the methane purification rate decreased with increasing turbine rotational speed, but the photocatalytic efficiency improved. In this research, the start of the PCR was set at the entrance of the collector, and it was cost-effective to lay 40 m in the radial direction with an investment of $4587 (around 0.37% of the total investment of the system). The system could degrade 30 595.47 g of atmospheric methane and reduce CO_2 emissions by 245.38 kg in the daytime in Wuhan. It was revealed that SCPP-PCR could be crucial for reducing greenhouse gas and limiting climate change.

KEYWORDS

CO_2 emissions reduction, greenhouse gas removal, methane photocatalysis, photocatalytic reactor, solar chimney

1 | INTRODUCTION

Methane, being the second-largest greenhouse gas, contributed significantly to global warming and climate change. The United Nations Environment Program (UNEP) stated that CH_4 emissions must be controlled to

Abbreviation: GWP, global warming potential; PCR, photocatalytic reactor; SCPP, solar chimney power plant; UNEP, United Nations Environment Program.

slow down global warming and climate change.[1] According to a UNEP report,[2] if the CH_4 emission could be effectively restricted, the global temperature could be reduced by 0.4°C to 0.5°C in 2050. Kretschmer et al[3] claimed that there were 114.6 billion tons of methane carbon dissolved in seawater, if the temperature of the deep ocean kept raising, methane carbon became unstable and decomposed. It was estimated that 473 tons of CH_4 would be escaped into the atmosphere within 100 years. In addition, considerable methane was emitted as a result of agriculture activities and the use of fossil fuels, accounting for nearly 60% of the total emission.[4] Although methane levels in the atmosphere were substantially lower than carbon dioxide (1.886 vs 415 ppm), CH_4 had a much larger global warming potential (GWP). Jackson et al[5] claimed the GWP of the CH_4 was 84 times that of CO_2 in the first 20 years after it was produced, and it was still 28 times that of CO_2 in the next 100 years. As a result, the total oxidation of atmospheric CH_4 to CO_2 removes 97% of the warming effect over a century time period, leading to significant climatic benefits.[5-7] Recently, several strategies for removing atmospheric CH_4 were described and compared in detail.[8]

Photocatalysis technology offered a promising way to remove the methane in the atmosphere. Electron–hole pairs would generate on the surface of the photocatalyst material under UV lamp, resulting in carboxyl active groups. The carboxyl groups could effectively oxidize the contaminants in the environment to non-toxic and innocuous substances.[9,10] Wada et al[11] conducted experimental research on methane, ethane, and propane photocatalytic reactions, and the results showed that methane was converted into carbon dioxide and a small amount of formaldehyde under UV irradiation. The amount of formaldehyde generated was primarily dependent on ultraviolet lamp irradiation intensity, time, and catalyst activity. Wada et al[12] found that the methane would be actively catalyzed and oxidized under UV irradiation with a wavelength less than 310 nm, producing methanol, CO_2, and H_2O. However, the production of water vapor would hinder the oxidation process of methane. When TiO_2 acted as the photocatalyst, Graetzel et al[13] claimed that the methane was effectively photocatalyzed to CO_2 and H_2O.

$$CH_4 + 2O_2 \xrightarrow{TiO_2} CO_2 + 2H_2O.$$

However, previous photocatalytic methane research was conducted solely in the laboratory but not in the field, because the environmental conditions, such as wind speed and direction, sun intensity, and humidity of the air, had impacts on the photocatalytic effect.[14]

The solar chimney power plant (SCPP) is a green power generation system consisting of a chimney, canopy, turbine, and storage layer. During the day, the sunlight passed through the canopy and heated the storage layer. The density of hot air in the SCPP was lower than that in the external environment, thus a strong flow was created in the system due to the stack effect.[15]

In 1982, the first SCPP was erected in Spain[16] and successfully ran for more than 7 years, demonstrating the possibility of generating electricity using the solar chimney (SC). Following then, researchers put many efforts to study SCPP. Bernardes et al[17,18] developed a numerical model and found that the chimney height, turbine construction, collector diameter, and material were the key parameters for SC design. Further, the entropy generation and the efficiency of the system were calculated.[19] Guo et al[20,21] established an unsteady CFD model for the thermodynamic analysis of the SCPP considering the thickness of storage layer, and obtained the optimal turbine pressure drop ratio by numerical simulation.[22] Since then, many research groups around the world studied the smaller prototypes experimentally. A SC with a 12.3 m tall tower and a 12.5 m radius canopy was constructed and tested in Belo Horizonte.[23] Kasaeian et al[24] developed a small SCPP and found the temperature inversion phenomena at the inlet of chimney. Koonsrisuk et al[25] used CFD model to study the optimal geometry parameters of the SCs. Zhou et al[26] built a theoretical model to analyze the heat transfer and fluid behaviors in a sloped-collector SCPP. Due to the low solar utilization efficiency of SCPP, researchers had developed several novel SCPPs with higher energy conversion efficiency or new functionalities. Maia et al[27-29] utilized small SCPP to dry agricultural products and developed theoretical models for thermodynamic analysis, demonstrating the practicality of this technology. Zuo et al[30] suggested the WSSCPPCSD technology and revealed that the system boosted the freshwater production and the power output significantly due to the special turbine at the chimney exit. In 2019, Jamali et al[31] proposed to combine semi-transparent photovoltaic (STPV) with SCPP to reduce the temperature of STPV. The convection of the canopy helped to cool the STPV and increase the power production efficiency of the system owing to the chimney effect. Some other innovative studies on SCPP[32-34] and accumulation of solar energy[35,36] were also worth noting.

de Richter et al[37] first time proposed the concept of integrating SCPP with photocatalytic reactors (PCR) for large-scale removal of non-CO_2 greenhouse gases from the atmosphere at the GHGR Conference in Oxford (UK) and a SCPP Conference (DE). He claimed that the SCPP-PCR could weaken the interference of environmental factors on the photocatalytic reaction, ensuring the continuous removal of atmospheric methane. The photocatalytic process of methane was mostly governed by the light intensity and concentration of methane, while

TABLE 1 Characteristics of different photocatalytic reactors

Types of PCR	Mass transfer rate	Reaction rate	Specific surface area
Plate	High	Medium	Low
Honeycomb	Medium	Low	High
Annular column	Low	High	Medium

temperature played a minor role.[38] Although the SCPP-PCR appeared to be a promising technique for the removal of methane from the atmosphere,[39,40] this had yet to be quantitatively evaluated or verified. In 2021, Ming et al[41] numerically studied the methane removal performance by the SCPP-PCR for the first time, where the TiO_2 was used to fill the photocatalytic reaction zone on honeycomb monolith. The effects of channel diameter, layer length, porosity, and solar radiation on the catalytic efficiency and purification rate were studied, providing invaluable information for the development of the SCPP-PCR prototype. However, due to the large press drop in the photocatalytic reaction zone, the flow rate inside the system was reduced by filling the porous PCR within the collector, which in turn impaired the output power. Thereby, it is hard to generate electricity via wind turbine installed in the SCPP.

Therefore, the purpose of this paper mainly includes the following two aspects: (a) Designing a simple structure of PCR to realize both the photocatalytic removal of non-CO_2 greenhouse gases and reducing CO_2 emissions through SCPP, so as to quantitatively verify the feasibility of the proposed SCPP-PCR concept by de Richter et al[37] (b) Further analyzing the relationship between the power output performance and the amount of methane removal under varying parameters in the SCPP-PCR. Herein, the photocatalytic zone was painted on the ground, and the effects of different solar radiation and rotational speeds of turbine on methane catalytic efficiency, purification rate, turbine output power, and CO_2 reduction were systematically studied by a three-dimensional numerical model.

2 | THEORETICAL MODELS

2.1 | Physics model

The model used in this study has the same geometric specifications as the Spanish SCPP prototype. The radius of the collector made of a transparent or translucent material is 120.0 m, the entrance is 2.0 m high, and the bottom of the chimney is 6.0 m high. The surface of the canopy, which has a slope of 1.9°, aiding in the airflow throughout the system and reduces energy loss. The height of the chimney made up of concrete is 200 m. The turbine is mounted 7.0 m above the ground. The turbine has four blades and uses CLARK-Y airfoils. The diameter of the impeller and the wheel is 9.8 and 2.1 m, respectively. And the space between the blade tip and the chimney wall is 0.1 m.[42]

The structure of PCR is the key element for the methane purification effect of the SCPP-PCR. The most extensively used structures are the plate,[43] honeycomb,[44] and annular column.[45] These reactors have different mass transfer rates, reaction rates, and specific surface areas. as shown in Table 1. The atmospheric methane concentration is low (about 1886 ppb). The SCPP can provide a vast reaction area to assure methane removal without compromising its power-generating impact. As a result, the plate PCR is adopted, and TiO_2, an effective and economical photocatalyst, is painted on the ground. The working principle of the SCPP-PCR is depicted in Figure 1.

2.2 | Numerical model

The following assumptions are made in the numerical modeling of the SCPP-PCR.

1. The system works in the steady-state.
2. The heat transfer within the photocatalyst layer is not considered.
3. The incompressible ideal gas model is used to simulate the gas density.[46]
4. The methane photocatalytic produces carbon dioxide and water, no other products.
5. The energy loss at the chimney-to-collector connection is not considered.

The fluid flow inside the SCPP-PCR is generated by natural convection, which is caused by the ambient air heated by the solar radiation. The strength of the buoyancy-induced flow can be judged by the Rayleigh number:

$$R_a = \frac{g\beta\Delta T H^3}{av}, \tag{1}$$

where g, β, a, and H are the gravitational acceleration (9.81 m^2/s), the thermal expansion coefficient, the thermal diffusivity, and the collector height, respectively. ΔT is the maximum temperature rise within the SCPP-PCR

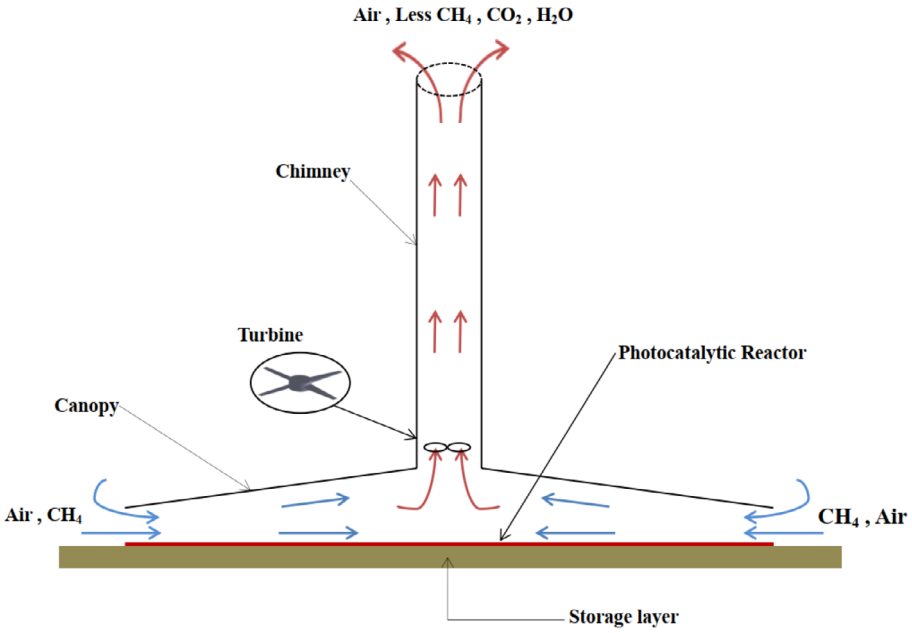

FIGURE 1 Schematic diagram of the SCPP-PCR system

and v is the kinematic viscosity, respectively. A rough calculation finds that Ra $>10^{10}$ in the chimney, indicating that the fluid flow reaches the turbulent state in the system. In fact, the k-ε model is the most commonly used turbulence model in the field of solar chimneys. The RNG k-ε model can better deal with flows owning a large swirl or curvature of streamline.[47] Therefore, the RNG k-ε model is adopted in this study. The governing equations, including the continuity equation, the momentum equations, the energy equation, the RNG k-ε equations, and the transport equations, are given as follows:

Continuity equation

$$\frac{\partial(\rho u_i)}{\partial x_i}=0. \tag{2}$$

Momentum equation

$$\frac{\partial(\rho u_i u_j)}{\partial x}=\rho g_i-\frac{\partial p}{\partial x_i}+\frac{\partial \tau_{ij}}{\partial x_j}. \tag{3}$$

Energy equation

$$\frac{\partial(\rho c_p u_j T)}{\partial x_j}=\frac{\partial}{\partial x_j}\left(\lambda\frac{\partial T}{\partial x_j}\right)+\tau_{ij}\frac{\partial u_i}{\partial x_j}+\beta T\left(\frac{\partial p}{\partial t}+u_j\frac{\partial p}{\partial x_j}\right). \tag{4}$$

Equation for the turbulent kinetic energy (k)

$$\frac{\partial}{\partial x_i}(\rho k u_i)=\frac{\partial}{\partial x_j}\left(\alpha_k\mu_{\text{eff}}\frac{\partial k}{\partial x_j}\right)+G_k+\rho\varepsilon. \tag{5}$$

Equation for the energy dissipation (ε)

$$\frac{\partial}{\partial x_i}(\rho\varepsilon u_i)=\frac{\partial}{\partial x_j}\left(\alpha_\varepsilon\mu_{\text{eff}}\frac{\partial \varepsilon}{\partial x_j}\right)+C_{1\varepsilon}\frac{\varepsilon}{k}G_k-C_{2\varepsilon}\rho\frac{\varepsilon^2}{k}. \tag{6}$$

Component transport equation

$$\nabla\cdot\left(\rho\overrightarrow{v}Y_i\right)=-\nabla\cdot\overrightarrow{J_i}+R_i+S_i, \tag{7}$$

where μ_{eff} ($\mu_{\text{eff}}=\mu+\mu_t$) represents the effective kinematic viscosity, G_k represents the generation of turbulence kinetic energy owing to buoyancy and can be defined as $G_k=-\rho\overline{u_i'u_j'}\frac{\partial u_j}{\partial x_i}$, α_k and α_ε are the turbulent Prandtl numbers for k and ε, respectively. Here, $\alpha_k=\alpha_\varepsilon=1.30$. $C_{1\varepsilon}$ and $C_{2\varepsilon}$ are two constants for the turbulent model with $C_{1\varepsilon}=1.44$, $C_{2\varepsilon}=1.92$. $\overrightarrow{J_i}$ represents the diffusion flux of species i, which is given by $\overrightarrow{J_i}=-\rho D_{i,m}+R_i$, where R_i represents the amount of component i produced or consumed in a chemical reaction, S_i represents the additional rate owing to the discrete phase, and Y_M indicates the variable dilatation incompressible turbulence contribution to the total dissipation rate.

The multiple reference frame (MRF) model is used to solve the turbine region. The MRF model provides a cost-effective solution for computation domains with moving parts. In the MRF model, the computational domain is broken down into several subdomains. Each subdomain owns specific motion mode, either stationary, rotating, or translational. The governing equations of the flow field in each subdomain are solved independently. Then, the flow field information in the nearby subdomains is exchanged at the interface by converting the velocity to absolute velocity. The velocity in the rotating coordinate system is given by

$$\vec{v_r} = \vec{v} - \vec{\omega} \times \vec{r}. \tag{8}$$

The governing equations of flow in the turbine region are given as follows:

Continuity equation

$$\nabla \cdot \left(\rho \vec{v_r}\right) = 0. \tag{9}$$

Momentum equations

$$\begin{aligned} &\nabla \cdot \left(\rho \vec{v_r} \vec{v_r}\right) + \rho\left(2\vec{\omega} \times \vec{v_r} + \vec{\omega} \times \vec{\omega} \times \vec{r}\right) + \rho \frac{\partial \vec{\omega}}{\partial t} \times \vec{r} \\ &= \nabla \cdot \left(\mu \nabla \vec{v_r}\right) + S_{\vec{v_r}}, \end{aligned} \tag{10}$$

where $\vec{v}$ is the absolute velocity, $\vec{\omega}$ is the angular velocity vector, and $\vec{r}$ is the position vector.

The output power (P_t) and the efficiency of the turbine (η) are calculated by Equation (11) and (12).

$$P_t = \frac{2\pi n M}{60}, \tag{11}$$

$$\eta = \frac{P_t}{\Delta p Q_v}, \tag{12}$$

where n represents the rotation speed, M represents the total blade moments, Q_v represents the volume flow rate of the system, and Δp represents the pressure drop of turbine.

Andreas et al[48] devised a set of experiments to derive an effective expression for the photocatalyzed total oxidation of methane:

$$r_{AI} = B \frac{B_1 c_1}{1 + B_1 c_1} \frac{B_2 c_2}{1 + B_2 c_2}, \tag{13}$$

where r_{AI} is the reaction rate of CH_4; c_1 is the concentration of CH_4; c_2 is the concentration of O_2; B, B_1, and B_2 are measured by experiments; and the parameter value are 5.37×10^{-7}, 2.42, and 4.60, respectively.

The photocatalytic efficiency and rate of methane are given by Equations (14) and (15).

$$\varepsilon_{\text{methane}} = \frac{J_1 - J_2}{J_1}, \tag{14}$$

$$\dot{m}_{\text{methane}} = Q_m (m_1 - m_2), \tag{15}$$

where J_1 and J_2 are the inlet and outlet methane concentrations, respectively; Q_m represents the mass flow rate of the system; and m_1 and m_2 are the mass fraction of methane at the entrance and exit, respectively.

3 | METHOD AND VALIDITY

3.1 | Meshing and independence verification

In the pre-processing, ICEM-CFD 19.2 is utilized for the meshing of SCPP-PCR. The computational domain is split into three sections: the canopy region, the turbine region, and the chimney region. A hybrid unstructured/structured grid system is implemented. In the turbine region, the chord length and blade installation angle vary with positions. As a result, in the turbine region, the unstructured grids are used, while the structured grids are generated in other areas. The grids near the blade surface are densified to improve the accuracy. Three grid systems with grid numbers of 6.65, 7.58, and 8.57 million, respectively, are used to check the grid independence. The volume flow rates at the outlet of the system are 698.457, 700.2578, and 706.3555 m^3/s, respectively, under the same environmental conditions, as shown in Table 2. A deviation of less than 1.0% demonstrates grid independence. Finally, the model with a total grid number of 7.58 million is adopted for the modeling. Table 3 shows the detail of grid information and Figure 2 depicts the grid diagram.

TABLE 2 Information of the grid independence

Grid numbers	6 654 174	7 584 953	8 576 342
Volume flow rates at the outlet of the system (m^3/s)	698.457	700.2578	706.3555

TABLE 3 Specific information of the grid

Region	Type	Grids ($\times 10^6$)	Minimum mesh quality
Canopy	Structured	2.403	0.75
Turbine	Unstructured	1.862	0.3
Chimney	Structured	3.721	0.9

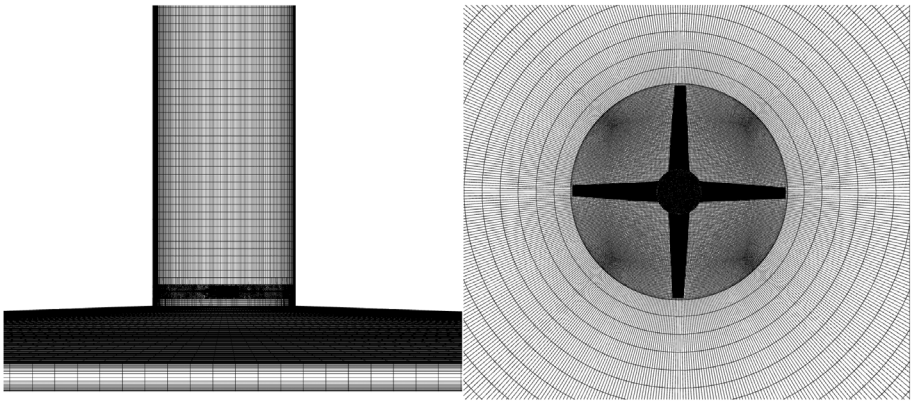

(A) (B)

FIGURE 2 Meshing of SCPP-PCR: (A) Front view of the grid and (B) Top view of the grid

TABLE 4 Boundary conditions

Location	Boundary type	Value
Collector inlet	Pressure inlet	$P = 0$ Pa, $T = 293$ K
Chimney outlet	Pressure outlet	$p = 0$ Pa
Ground surface	Heat flux	$q = 200\text{-}600$ W/m^2
Collector canopy surface	convection	$T = 293$ K, $h = 10$ W/(m^2·K)
Chimney wall	Adiabatic wall	$q = 0$ W/m^2
Turbine rotational speed		$\omega = 60\text{-}200$ rpm

3.2 | Boundary conditions and numerical solution

The ANSYS FLUENT 19.2 is utilized for the numerical solution. Table 4 shows the boundary conditions in the computational domain. In the SCPP-PCR, the entrance and exit of the SCPP-PCR are set as pressure inlet and pressure outlet, respectively. The inlet temperature is assumed to be the same as the ambient temperature (293.15 K). The relative pressures at the entrance and exit are both preset at 0 Pa.[49] When the ambient wind speed does not exceed 2 m/s, the collector surface is considered as a convective boundary condition, with a convective coefficient of 10 W/(m^2·K).[50] The wall of the chimney is regarded as an adiabatic boundary. In the turbine domain, a MRF model is used, with two interfaces combining the rotating and stationary regions. The wall boundaries are set as no-slip walls. The solar radiation is adjusted to the ground surface heat flux after accounting for the heat loss. According to solar radiation data from the desert in northwest China,[51] the heat flux of the ground is 600 W/m^2 under the canopy, accounting for $G = 857$ W/m^2. Assuming that the SCPP-PCR is established in Wuhan, China, the solar radiations for case studies are set to be 285.7, 428.5, 571.4, 714.2, and 857 W/m^2, respectively. The corresponding heat flux of the ground is 200, 300, 400, 500, and 600 W/m^2.

The Boussinesq approximation[52] and incompressible ideal gas model[46] are commonly used density models to solve natural convection. According to Boussinesq approximation, the air density is made up of the sum of the reference density term (ρ_0) and the density change term ($\Delta\rho$) owing to temperature, but this does not apply to multicomponent gases. In this paper, the incompressible ideal gas model is used to simulate the air density in SCPP-PCR due to the photocatalytic reaction of methane. The density calculation formula is: $\rho = \frac{p_{op}}{RT}$ and is only related to temperature. The RNG k-ε model is selected taking into consideration the buoyancy effect.

For photocatalytic reactions, the chemical reactions occur solely on the surface of photocatalysts (TiO_2). To characterize the rate of chemical reaction, a finite-rate reaction model is adopted. The rate of component convective diffusion to the surface and surface consumption formation is used to compute the concentration of each component at the reaction surface. Only a layer of grid near the photocatalyst surface is involved in the photocatalytic surface reaction. Convective transfer of methane along the vertical direction of the reactor surface is relatively small compared to diffusive transfer because the fluid velocity near the ground is very small. The double precision solver is utilized in numerical calculation. The PRESTO! discretization scheme is used for pressure term. The second-order upwind scheme is employed for the other terms. The SIMPLEC algorithm is adopted for pressure–velocity coupling. The solution is thought converged when the residuals of each equations are less than 10^{-5}.

TABLE 5 Comparison of numerical simulation data with experimental data

Parameters	Experimental data	Numerical simulation date	Tolerance
Maximum temperature rise (K)	17.5	18.7	6.9%
Chimney outlet velocity (m/s)	9	8.97	0.3%
Output power of turbine (kW)	36	37.86	5.2%

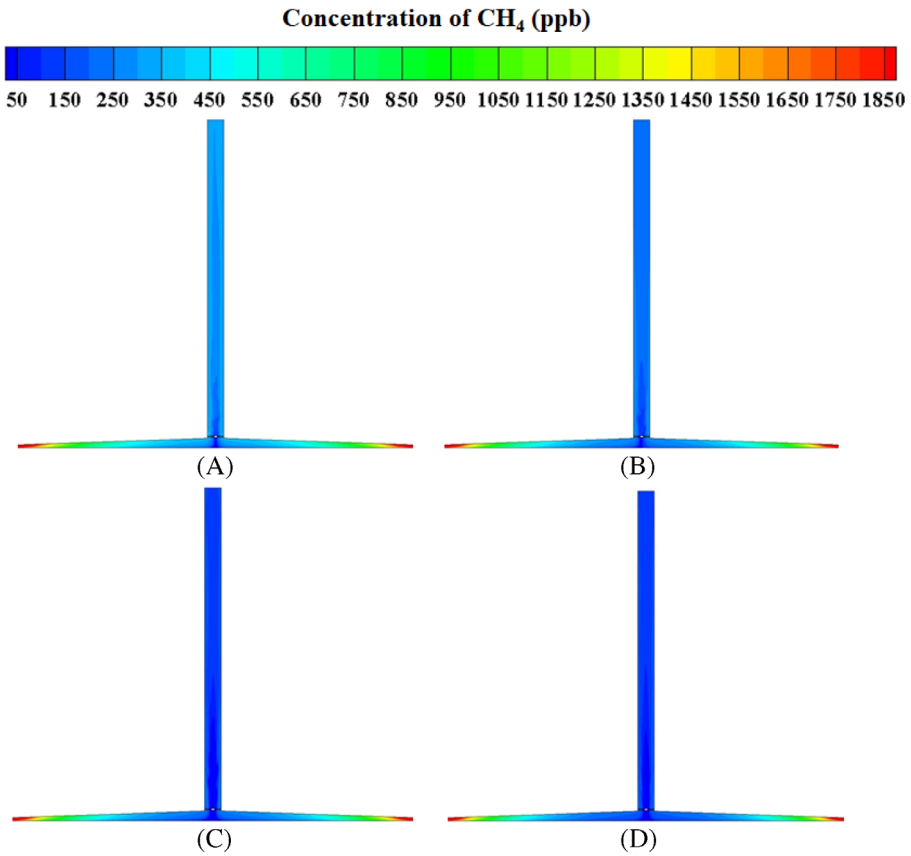

FIGURE 3 Contours of the CH_4 concentration in the axial plane of the system with $G = 857$ W/m^2. (A) $n = 80$ rpm, (B) $n = 100$ rpm, (C) $n = 120$ rpm, (D) $n = 140$ rpm

3.3 | Validation of numerical simulations

According to experimental data supplied by Haaf,[53] when $G = 800$ W/m^2 and $n = 100$ rpm, the outlet velocity of the chimney is 9 m/s, the output power of the turbine is 36 kW, and the maximum temperature rise in the system is 17.5 K. In the validation procedure, the environmental conditions of the numerical model are set the same to the experiment of Haff, the results show that the system outlet velocity is 8.97 m/s, the turbine output power is 37.86 kW, and the maximum temperature rise in the system is 18.7 K. As is shown in Table 5, the relative error between the experimental and modeling results is less than 6.9%. The temperature rise and output power of the system are higher than the experimental result because the heat loss through the wall of the SC is neglected.[18] Overall, the numerical results match well with the experimental data, confirming the accuracy of the numerical simulation approach.

4 | RESULTS AND DISCUSSION

The temperature, velocity, and pressure fields inside SCPP have not varied appreciably as a layer of photocatalyst is coated on the ground in this paper. The fluid field analysis is not presented because there have been some published studies on this.[54] This paper focuses on the methane distribution, the capacity to degrade atmospheric methane, and the photoreactor reaction rate of the SCPP-PCR. Furthermore, the atmospheric CH_4 degradation potential is compared to that of SCPP integrated with honeycomb photoreactor,[41] and CO_2 emission reduction is briefly analyzed.

4.1 | Atmospheric methane degradation

Figure 3 shows contours of the CH_4 concentration in the axial plane of the system when $G = 857$ W/m^2 with

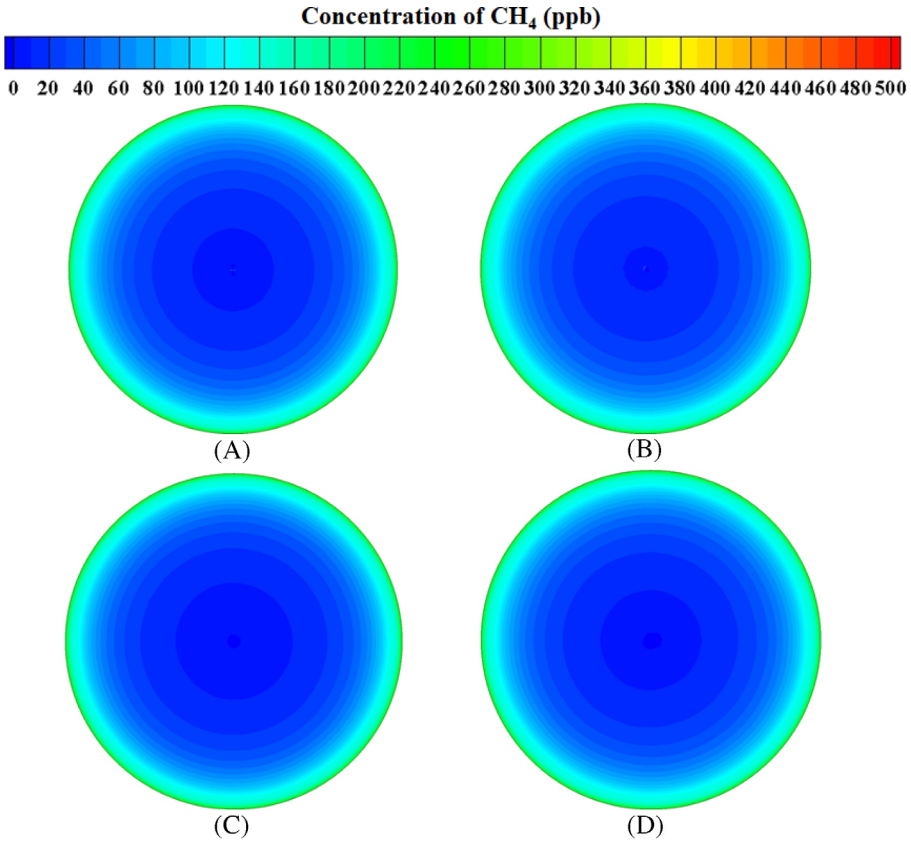

FIGURE 4 Contours of the CH_4 concentration 0.01 m above the ground with $G = 857$ W/m^2. (A) $n = 80$ rpm, (B) $n = 100$ rpm, (C) $n = 120$ rpm, (D) $n = 140$ rpm

different turbine rotational speeds. The methane concentration in the atmosphere is 1886 ppb. Because of the stack effect caused by the SCPP, the methane is continually sucked into the system. The oxidation reaction occurs when the CH_4 contacts with the titanium dioxide painted on the ground under solar radiation. The CH_4 is continually degraded on the ground in the radial direction of the collection. The air velocity in the collector is very small, thus the mass convective process is relatively weak. The methane in the mainstream has to diffuse down to be degraded on the photocatalyst surface. The methane concentration under the wheel is zero. The rotation of the turbine continues to impact the distribution of methane inside the system after it passes through the turbine. But the methane distribution becomes more uniform as the flow moves upward. The concentration of the methane at the exit is 269.2 ppb, about 14.2% of that in the atmosphere.

When the speeds of the turbine rotational are 100, 120, and 140 rpm, respectively, the corresponding methane concentration at the output is 226.0, 144.8, and 141.5 ppb, respectively. The methane content at the exit drops with the increase of turbine rotational speed. Simultaneously, the turbine rotation speed has a substantial impact on the distribution of methane in the chimney. The slower the rotation speed, the faster the methane is mixed uniformly.

Figure 4 shows contours of the CH_4 concentration 0.01 m above the ground painted with photocatalyst when $G = 857$ W/m^2. The concentration gradient in the radial direction of the collector is considerable due to the photocatalytic reaction. It is found that the methane concentration drops faster at the reactor entrance of the reactor. The reaction rate of methane is relatively fast in this region where the concentration of methane is high and the flow velocity there is very slow.

The photocatalytic efficiency and purification rate of the methane are used to characterize the CH_4 removal performance of the SCPP-PCR. Figure 5 shows the effect of turbine rotational speed on the photocatalytic efficiency of CH_4. The rate of electron and hole creation is impacted by the intensity of the light, which in turn influences the rate of photocatalytic reaction.[55] When the rate of electron and hole creation exceeds that of the photocatalytic reaction, the rate of the reaction is independent of light intensity and is primarily influenced by mass transfer rate. In the SCPP-PCR, the complex cooperative process of mass transfer is influenced by both solar radiation and turbine rotation. When $G = 428.5$ W/m^2, the airflow velocity in the system is moderate, and mass transfer rate on the surface of the photocatalyst is influenced by the turbine speed. The mass transfer rate between 100 and 120 rpm is greatly increased, as well as the methane photocatalytic efficiency.

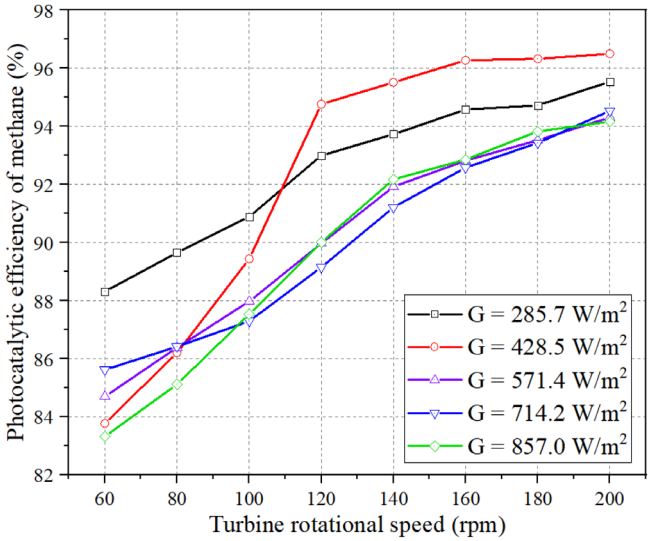

FIGURE 5 Effect of turbine rotational speed on photocatalytic efficiency of methane

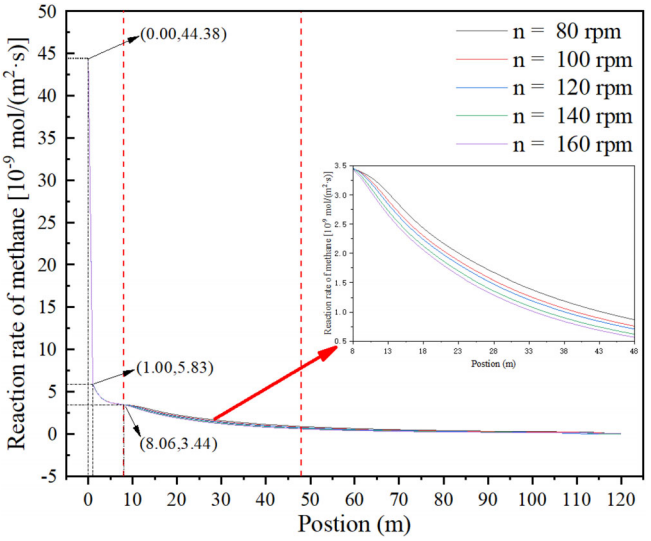

FIGURE 7 Photocatalytic reaction rate on the surface of catalyst with various turbine rotational speeds under $G = 857$ W/m^2

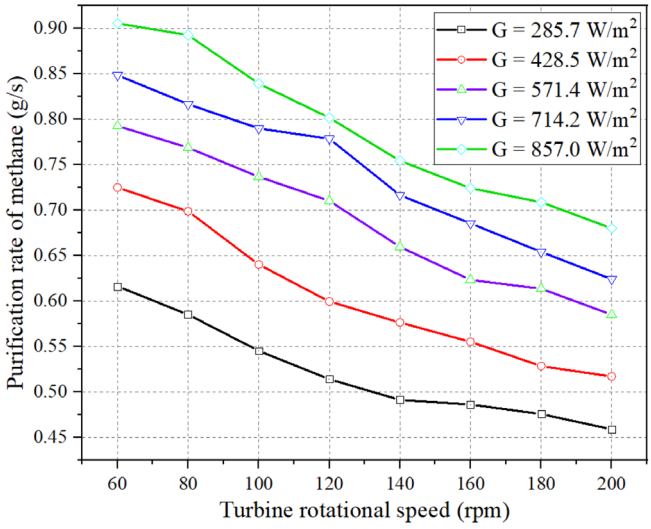

FIGURE 6 Effect of turbine rotational speed on purification rate of methane

Figure 6 shows the influence of turbine rotational speed on the purification rate of methane. As the rotating speed of the turbine increases, the rate of methane purification drops, photocatalytic efficiency improves, but the mass flow rate of SCPP-PCR is decreased. It can be noticed that the mass flow rate of the system has a more significant impact on the methane purification rate. And the quantity of methane degradation per unit time is relatively high under high solar radiation. For example, the maximum purification rate of CH_4 of the SCPP-PCR is 0.905 g/s when $G = 857$ W/m^2.

4.2 | Reaction rate in photoreactor

Furthermore, considering the initial investment cost of PCR, it is critical to investigate the reaction rate inside the PCR to determine the titanium dioxide laying length. The reaction rates on the surface of catalyst with various turbine rotational speeds with $G = 857$ W/m^2 are as illustrated in Figure 7. The reaction rate reduces drastically within 1 m of the reactor entrance and then keeps at a low level. Though the rotational speed varies, the reaction rate remains almost constant within 8.06 m of the entry, peaking at 44.39×10^{-9} mol/(m^2·s) at the entrance, and 3.44×10^{-9} mol/(m^2·s) at 8.06 m. The lower the turbine rotational speed, the higher the reaction rate after 8.06 m in the same position. This is due to the fact that the concentration of methane is high and the contact time with the photocatalyst is lengthy in the first 8.06 m at the reactor entrance; therefore, the reaction rate is basically the same. After 8.06 m, the lower the turbine rotational speed, the higher the mass flow rate of the system, that is, the more methane enters the system per unit time. In this case, the methane concentration is slightly higher, which results in a slightly higher reaction rate.

Figure 8 shows the CH_4 reaction rate on the surface of the catalyst with different solar radiations under a turbine rotational speed of 100 rpm. It shows that the higher the solar radiation, the faster the reaction rate is at the same position. The reaction rate of CH_4 declined dramatically within 1 m of the reactor entrance, despite differences in the solar radiation intensity. The maximum

reaction rates at the inlet are 44.39, 36.99, 29.59, 22.19, and 17.49 $\times 10^{-9}$ mol/(m^2·s), respectively, when solar radiation is 285.7, 428.5, 571.4, 714.2, and 857 W/m^2, respectively. The photocatalytic reaction rate is lower than 1×10^{-9} mol/(m^2·s) at the position 40 m away from the entrance. If the start of the PCR is placed at the entrance of the system, it is cost-effective to paint the photocatalyst for the first 40 m in the radial direction, giving the photocatalytic reaction zone a total area of 25 132.74 m^2.

4.3 | Comparison of different types of photoreactor

The types of photoreactors have significant influence on the ability of the system to degrade atmospheric methane. According to the numerical simulation results,[41] in the case of no load, the photocatalytic efficiency of methane can be improved to more than 95% by extending the length of the reaction zone, despite the use of honeycomb reactors with variable pore diameters. Therefore, the comparison of methane photocatalytic effects between SCPP with plate photoreactor or the honeycomb photoreactor ($d_{pore} = 4$ mm) system is shown in Table 6, under $G = 857$ W/m^2.

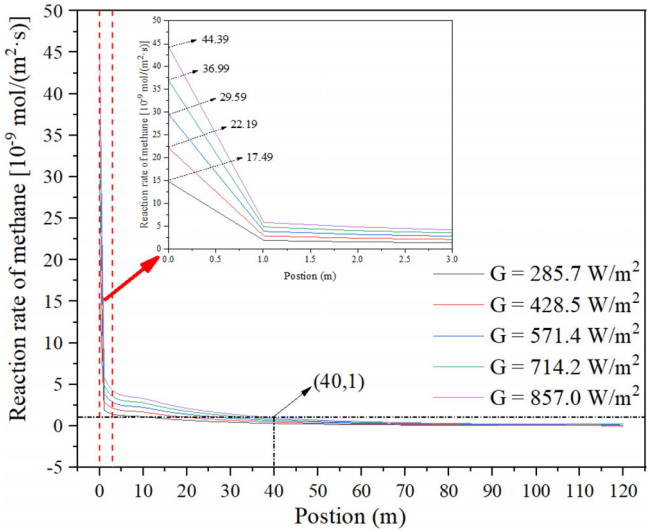

FIGURE 8 Photocatalytic reaction rate on the surface of catalyst with various solar radiation under $n = 100$ rpm

The methane will stay on the catalyst surface longer if the turbine rotation speed or the length of the honeycomb PCR is increased, resulting in more complete catalysis. Though increasing the length of the honeycomb improves methane catalytic efficiency, the long reactor creates a large pressure drop, reducing the mass flow rate of the SCPP-PCR and resulting in a poor methane purification rate. For example, when the length of the honeycomb reactor is 8 m, the catalytic efficiency of methane is 93.46%, and the pressure drop is 149.99 Pa, resulting a purification rate of 0.68 g/s. Though the catalytic efficiency of the plate photoreactor is increased to 97.03% when the reactor length is extended to 10 m, the methane purification rate reduced to 0.66 g/s as the mass flow of the system is significantly reduced.

The methane photocatalytic process is normally carried out in numerous phases.[56] The honeycomb photoreactor can achieve full oxidation of methane by prolonging the reaction time. However, the large internal pressure drop in the honeycomb photoreactor restricts the power output of the SCPP. In this paper, both the complete oxidation of methane and power generation are of great importance to reduce CO_2 emissions. It is thought that a SCPP integrated with a plate photoreactor is more ideal, as it can not only purify methane but also create energy.

TABLE 6 Degradation of atmospheric methane by coupling different types of photoreactors

Plate			Honeycomb			
Turbine rotational speed (rpm)	Photocatalytic efficiency (%)	Purification rate (g/s)	Length of the PCR (m)	Photocatalytic efficiency (%)	Purification rate (g/s)	Pressure of the PCR (Pa)
60	83.32	0.91	3	59.46	0.52	80.45
80	85.12	0.89	4	71.26	0.59	97.48
100	87.53	0.84	5	80.11	0.63	110.53
120	90.01	0.80	6	86.23	0.66	123.92
140	92.18	0.75	7	90.38	0.67	138.99
160	92.86	0.72	8	93.46	0.68	149.99
180	93.83	0.71	9	95.59	0.67	160.29
200	94.17	0.68	10	97.03	0.66	169.87

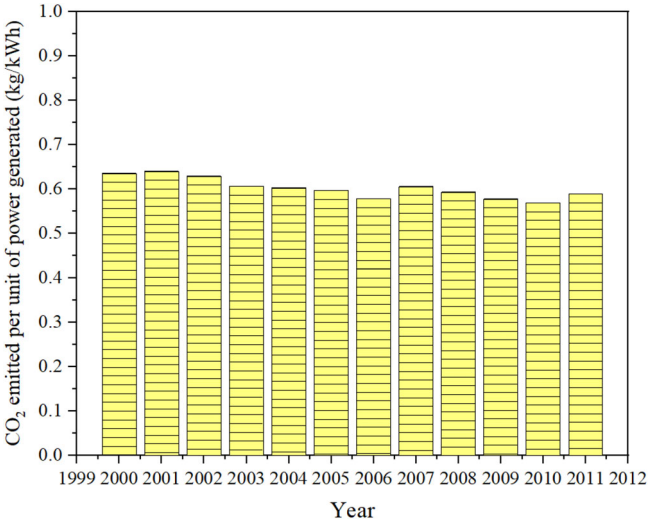

FIGURE 9 CO_2 emissions from thermal power plant unit power generation

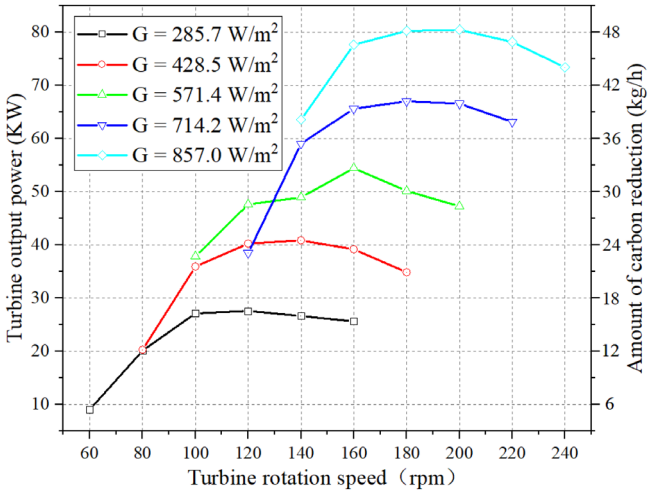

FIGURE 10 Variation curves of turbine output power and CO_2 reduction

4.4 | CO_2 emission reduction technology

Hydropower, thermal power, and nuclear power were the primary sources of electricity at the end of the 1980s.[57] The position of the three primary kinds differed depending on countries. At the moment, thermal power generation dominates the world, accounting for more than 70% of overall power generation. Thermal power is created by burning fuel, which emits tremendous CO_2. Muangthai et al[58] investigated the relation of power generation and carbon dioxide emission of thermal power plant in Thailand, and the link between calculated unit power generation and carbon dioxide emission is presented in Figure 9. They found that 0.6 kg of carbon dioxide is released from a thermal power plant for every 1 kWh of electricity produced.

The SCPP is a green system that generates electricity from solar energy without emitting CO_2. Figure 10 depicts the influence of turbine rotation speed on turbine output power and CO_2 emission reduction under various solar radiation conditions. They both follow the same pattern, rising first and then falling. With the turbine rotational speed increases, the mass flow rate of the system falls, resulting in a drop in the torque of the blade. The output power of a turbine is the product of the turbine rotational speed and the torque, which reaches a peak value at certain turbine rotational speed. The increase in solar radiation improves the output power of SCPP-PCR, easing the burden on the thermal power plant and reducing CO_2 emissions. For example, turbine output power reaches a maximum of 80.49 kW and carbon dioxide emission reduction is 48.29 kg/h when solar radiation is 857 W/m^2 and turbine rotation speed is 200 rpm. Electricity produced from non-fossil fuels utilizing such a clean power generation system reduces CO_2 emissions significantly.

5 | DISCUSSION

This study is inspired by the limits of present methods to tackle global warming. The investment of the SCPP-PCR and the methane degradation capability are estimated as follows.

It costs around $1.25 million to build the SCPP, including the costs for glass, concrete, power equipment (turbines, gearboxes, and power generators), and installation.[59] P25 is a white nano-sized titanium dioxide powder with a density of 3900 kg/m^3 and a particle size of 25 nm in average. It is a cost-effective photocatalyst with a long lifetime, high stability, and difficult deactivation properties.[60] In the SCPP system, the P25 is painted on the ground. To achieve the best photocatalytic effect, the PCR is expected to consume 50 g photocatalyst per square meter.[37] For a SCPP-PCR with a reaction zone of 25 132.74 m^2, a total of 1.39 tons of photocatalyst paint is used. The current price of P25 powder is $3300 per ton;[37] therefore, the total investment of the PCR is about $4587, approximately 0.37% of the total investment of the SCPP-PCR system.

The calculation is done based on the solar radiation data of Wuhan on July 17, 2011.[61] The solar radiations from 6:00 A.M. to 6:00 P.M., with the corresponding values are 155, 535, 820, 883, 720, and 385 W/m^2, respectively, are input data for the analysis. Table 7 shows the volume flow rate, methane purification rate, output power of turbine, and CO_2 reduction of the SCPP-PCR when $n = 100$ rpm.

TABLE 7 Calculation results in Wuhan on July 17, 2011

Time (Local Beijing time) (July 17, 2011)	Solar radiation (2 hours average) (W/m^2)	Volume flow rate (m^3/s)	Methane purification rate (g/s)	The output power of turbine (kW)	The CO_2 reduction (kg/h)
6:00 AM–8:00 AM	155	397.49	0.44	16.48	9.89
8:00 AM–10:00 AM	535	682.87	0.70	37.83	22.70
10:00 AM–12:00 AM	820	841.79	0.84	38.27	22.96
12:00 AM–2:00 PM	883	847.12	0.87	39.76	23.86
2:00 PM–4:00 PM	720	784.04	0.79	38.47	23.08
4:00 PM–6:00 PM	385	575.88	0.61	33.67	20.20

The simulations demonstrate that the SCPP-PCR can degrade methane in the atmosphere on a large scale. The system can reduce 245.38 kg CO_2 emissions generated from thermal power in the daytime. Furthermore, the system can process 29 730 199.61m^3 of air and purify 30 595.47 g of methane in 1 day, which can significantly mitigate the greenhouse effect. The methane purification rate can be further enhanced by developing a night operation strategy. For example, the SCPP can work continuously by employing a heat storage layer, and the ultraviolet irradiation for the photocatalysis can be provided by the electricity generated by the SCPP itself. In this way, the methane purification rate might be doubled.[39]

6 | CONCLUSION

In this study, the photocatalytic performance and the carbon dioxide reduction of the SCPP-PCR are analyzed by conducting three-dimensional steady-state CFD simulations. The feasibility of the SCPP-PCR for both clean electricity generation and large-scale methane removal is analyzed. The following are conclusions:

1. The SCPP integrated with plate photoreactor is more optimal than a honeycomb photoreactor when neglecting the influence of the wind environment on the system. The honeycomb photoreactor provides higher methane conversion efficiency, but correspondingly high internal resistance. Meanwhile, the plate photoreactor provides both considerable methane purification rate and produce power.
2. The reaction rate reduces drastically within 1 m of the entrance of the PCR and then slows down gradually. It is cost-effective to paint the photocatalyst at the entrance of the SCPP for the first 40 m along the radial direction.
3. According to the simulation results, the photocatalytic efficiency increases with the turbine rotational speed and the maximum efficiency reaches 96.5%. However, the methane purification rate decreases with the turbine rotational speed and the maximum rate is 0.91 g/s. The system can process 29 730 199.61m^3 of air, purify 30 595.47 g of methane, and reduce CO_2 emissions by 245.38 kg in a day at Wuhan, China.

NOMENCLATURE

n	turbine rotational speed, rpm
B, B_1, B_2	experimental parameter value
$C_{1\varepsilon}$, $C_{2\varepsilon}$	constants for turbulent model
Q_m	mass flow rate, $kg{\cdot}s^{-1}$
c_1	CH_4 concentration, $mol{\cdot}m^{-3}$
c_2	O_2 concentration, $mol{\cdot}m^{-3}$
$\varepsilon_{\text{methane}}$	photocatalytic efficiency
$\dot{m}_{\text{methane}}$	purification rate, $g{\cdot}s^{-1}$
G	solar radiation, $W{\cdot}m^{-2}$
$\overrightarrow{J_i}$	diffusion flux of species i, $mol{\cdot}s^{-1}{\cdot}m^{-3}$
J_1	methane concentration at system entrance, $mol{\cdot}m^{-3}$
J_2	methane concentration at system exit, $mol{\cdot}m^{-3}$
M	total blade moments of the turbine, $N{\cdot}m^{-1}$
q	heat flux, $W{\cdot}m^{-2}$
R_a	rayleigh number
P_t	turbine output power, kW
r_{AI}	reaction rate of CH_4, mol $W^{-1}{\cdot}s^{-1}$
Δp	drop across the turbine, Pa
S_Φ	momentum loss term
S_i	additional rate owing to the discrete phase
m_1	mass fraction of methane at the SC entrance
m_2	mass fraction of methane at the SC exit
x, y, z	Cartesian space coordinates

Greek Symbols

ν	kinetic viscosity, $m^2{\cdot}s^{-1}$
β	coefficient of thermal expansion, K^{-1}
ρ	glass density, $kg{\cdot}m^{-3}$
τ	shear stress, $N{\cdot}m^{-2}$
k	Karman constant
η	efficiency of the turbine

ACKNOWLEDGEMENTS

This research was supported by the National Key Research and Development Plan (Key Special Project of Inter-governmental National Scientific and Technological Innovation Cooperation, Grant No. 2019YFE0197500), National Natural Science Foundation of China (Grant No. 51778511), the European Commission H2020 Marie Curie Research and Innovation Staff Exchange (RISE) award (Grant No. 871998), Key Research and Development Projects of Hubei Province (Grant No. 2020BAB129), and the Scientific Research Foundation of Wuhan University of Technology (Grant Nos. 40120237 and 40120551).

DATA AVAILABILITY STATEMENT

The data that support the findings of this study are available from the corresponding author upon reasonable request.

REFERENCES

1. Zhongming Z, Linong L, Wangqiang Z, Wei L. Near-term climate protection and clean air benefits: actions for controlling short-lived climate forcers-a UNEP synthesis Report 2011.
2. Blok K, Hare W, Hohne N, et al. Bridging the emissions gap: a UNEP synthesis report. United Nations Environment Programme (UNEP). 2011.
3. Kretschmer K, Biastoch A, Rüpke L, Burwicz E. Modeling the fate of methane hydrates under global warming. *Global Biogeochem Cycles*. 2015;29(5):610-625.
4. Saunois M, Stavert AR, Poulter B, et al. The global methane budget 2000–2017. *Earth Syst Sci Data*. 2020;12(3):1561-1623.
5. Jackson RB, Solomon EI, Canadell JG, Cargnello M, Field CB. Methane removal and atmospheric restoration. *Nat Sustain*. 2019;2(6):436-438.
6. Jackson RB, Abernethy S, Canadell JG, et al. Atmospheric methane removal: a research agenda. *Philos Trans A Math Phys Eng Sci*. 2021;379(2210):20200454.
7. Nisbet-Jones PBR, Fernandez JM, Fisher RE, et al. Is the destruction or removal of atmospheric methane a worthwhile option? *Philos Trans A Math Phys Eng Sci*. 2022;380(2215):20210108.
8. Ming T, Li W, Yuan Q, et al. Perspectives on removal of atmospheric methane. *Adv Appl Energy*. 2022;5:100085.
9. Liu L, Yang W, Li Q, Gao S, Shang JK. Synthesis of Cu_2O nanospheres decorated with TiO_2 nanoislands, their enhanced photoactivity and stability under visible light illumination, and their post-illumination catalytic memory. *ACS Appl Mater Interfaces*. 2014;6(8):5629-5639.
10. Pelaez M, Nolan NT, Pillai SC, et al. A review on the visible light active titanium dioxide photocatalysts for environmental applications. *Appl Catal B Environ*. 2012;125:331-349.
11. Wada K, Yoshida K, Takatani T, Watanabe Y. Selective photo-oxidation of light alkanes using solid metal oxide semiconductors. *Appl Catal A Gen*. 1993;99(1):21-36.
12. Wada K, Yamada H, Watanabe Y, Mitsudo T-a. Selective photo-assisted catalytic oxidation of methane and ethane to oxygenates using supported vanadium oxide catalysts. *J Chem Soc Faraday Trans*. 1998;94(12):1771-1778.
13. Graetzel M, Thampi K, Kiwi J. Methane oxidation at room temperature and atmospheric pressure activated by light via polytungstate dispersed on titania. *J Phys Chem*. 1989;93(10):4128-4132.
14. Dylla H, Hassan MM, Osborn D. Field evaluation of ability of photocatalytic concrete pavements to remove nitrogen oxides. *Transp Res Rec*. 2012;2290(1):154-160.
15. Cottam P, Duffour P, Lindstrand P, Fromme P. Solar chimney power plants–dimension matching for optimum performance. *Energy Convers Manag*. 2019;194:112-123.
16. Haaf W, Friedrich K, Mayr G, Schlaich J. Solar chimneys part I: principle and construction of the pilot Plant in Manzanares. *Int J Solar Energy*. 2007;2(1):3-20.
17. Bernardes M, Valle RM, Cortez FB. Numerical analysis of natural laminar convection in a radial solar heater. *Rev Gén Therm*. 1999;38(1):42-50.
18. Bernardes M, Voß A, Weinrebe G. Thermal and technical analyses of solar chimneys. *Sol Energy*. 2003;75(6):511-524.
19. Koonsrisuk A. Comparison of conventional solar chimney power plants and sloped solar chimney power plants using second law analysis. *Sol Energy*. 2013;98:78-84.
20. Guo P, Wang Y, Li J, Yuan W. Thermodynamic analysis of a solar chimney power plant system with soil heat storage. *Appl Therm Eng*. 2016;100:1076-1084.
21. Guo P-h, Li J-y, Wang Y. Numerical simulations of solar chimney power plant with radiation model. *Renew Energy*. 2014;62:24-30.
22. Guo P, Li J, Wang Y, Wang Y. Evaluation of the optimal turbine pressure drop ratio for a solar chimney power plant. *Energy Convers Manag*. 2016;108:14-22.
23. Maia CB, Castro Silva JO, Cabezas-Gómez L, Hanriot SM, Ferreira AG. Energy and exergy analysis of the airflow inside a solar chimney. *Renew Sust Energ Rev*. 2013;27:350-361.
24. Kasaeian AB, Heidari E, Vatan SN. Experimental investigation of climatic effects on the efficiency of a solar chimney pilot power plant. *Renew Sust Energ Rev*. 2011;15(9):5202-5206.
25. Koonsrisuk A, Chitsomboon T. Mathematical modeling of solar chimney power plants. *Energy*. 2013;51(51):314-322.
26. Zhou X, Yuan S, Bernardes MAS. Sloped-collector solar updraft tower power plant performance. *Int J Heat Mass Transf*. 2013;66:798-807.
27. Ferreira AG, Maia CB, Cortez MFB, Valle RM. Technical feasibility assessment of a solar chimney for food drying. *Sol Energy*. 2008;82(3):198-205.
28. Maia CB, Ferreira AG, Cabezas-Gómez L, Silva JOC, de Morais HS. Thermodynamic analysis of the drying process of bananas in a small-scale solar updraft tower in Brazil. *Renew Energy*. 2017;114:1005-1012.
29. Maia CB, Silva JDC. Thermodynamic assessment of a small-scale solar chimney. *Renew Energy*. 2022;186:35-50.
30. Zuo L, Ding L, Chen J, Zhou X, Xu B, Liu Z. Comprehensive study of wind supercharged solar chimney power plant combined with seawater desalination. *Sol Energy*. 2018;166:59-70.
31. Jamali S, Nemati A, Mohammadkhani F, Yari M. Thermal and economic assessment of a solar chimney cooled semi-transparent photovoltaic (STPV) power plant in different climates. *Sol Energy*. 2019;185:480-493.

32. Ashouri M, Hakkaki-Fard A. Improving the performance of the finned absorber inclined rooftop solar chimney combined with composite PCM and PV module. *Sol Energy*. 2021;228: 562-574.
33. Saad M, Ahmed N, Mahmood M, Sajid MB. Performance enhancement of solar updraft tower plant using parabolic chimney profile configurations: a numerical analysis. *Energy Rep*. 2022;8:4661-4671.
34. Sengupta A, Mishra DP, Sarangi SK. Computational performance analysis of a solar chimney using surface modifications of the absorber plate. *Renew Energy*. 2022;185:1095-1109.
35. Zhao X, Chen Z, Yan S, Ming T, Wu Z, Ma R. Influence of dust accumulation on the solar reflectivity of a linear Fresnel reflector. *J Therm Sci*. 2020;30(5):1526-1540.
36. Zhao N, Yan S, Ma X, et al. Analysis of the light concentration loss of a Fresnel CPV/T system after dust accumulation. *J Therm Sci*. 2021. doi:10.1007/s11630-021-1466-8
37. Ming T, Davies P, Liu W, Caillol S. Removal of non-CO_2 greenhouse gases by large-scale atmospheric solar photocatalysis. *Prog Energy Combust Sci*. 2017;60:68-96.
38. Chen X, Li Y, Pan X, Cortie D, Huang X, Yi Z. Photocatalytic oxidation of methane over silver decorated zinc oxide nanocatalysts. *Nat Commun*. 2016;7(1):1-8.
39. Ming T, de Richter R, Shen S, Caillol S. Fighting global warming by greenhouse gas removal: destroying atmospheric nitrous oxide thanks to synergies between two breakthrough technologies. *Environ Sci Pollut Res*. 2016;23(7):6119-6138.
40. Ming T, Caillol S, Liu W. Fighting global warming by GHG removal: destroying CFCs and HCFCs in solar-wind power plant hybrids producing renewable energy with no-intermittency. *Int J Greenhouse Gas Control*. 2016;49:449-472.
41. Ming T, Gui H, Shi T, et al. Solar chimney power plant integrated with a photocatalytic reactor to remove atmospheric methane: a numerical analysis. *Sol Energy*. 2021;226:101-111.
42. Tingzhen M, Wei L, Guoling X, Yanbin X, Xuhu G, Yuan P. Numerical simulation of the solar chimney power plant systems coupled with turbine. *Renew Energy*. 2008;33(5):897-905.
43. Yang R, Zhang Y, Xu Q, Mo J. A mass transfer based method for measuring the reaction coefficients of a photocatalyst. *Atmos Environ*. 2007;41(6):1221-1229.
44. Hossain MM, Raupp GB, Hay SO, Obee TN. Three-dimensional developing flow model for photocatalytic monolith reactors. *AICHE J*. 1999;45(6):1309-1321.
45. Doucet N, Zahraa O, Bouchy M. Kinetics of the photocatalytic degradation of benzene. *Catal Today*. 2007;122(1–2):168-177.
46. Rahbar K, Riasi A. Performance enhancement and optimization of solar chimney power plant integrated with transparent photovoltaic cells and desalination method. *Sustain Cities Soc*. 2019;46:101441.
47. Kasaeian A, Mahmoudi AR, Astaraei FR, Hejab A. 3D simulation of solar chimney power plant considering turbine blades. *Energy Convers Manag*. 2017;147:55-65.
48. Haeger A, Kleinschmidt O, Hesse D. Kinetics of photocatalyzed gas reactions using titanium dioxide as the catalyst part II: Photocatalyzed total oxidation of alkanes with oxygen. *Chem Eng Technol: Ind Chem-Plant Equip-Process Eng-Biotechnol*. 2004;27(9):1019-1026.
49. Cuce E, Saxena A, Cuce PM, et al. Performance assessment of solar chimney power plants with natural thermal energy storage materials on ground: CFD analysis with experimental validation. *Int J Low-Carbon Technol*. 2022;17:752-759.
50. Tingzhen M, Wei L, Guoliang X. Analytical and numerical investigation of the solar chimney power plant systems. *Int J Energy Res*. 2006;30(11):861-873.
51. Ming T, Wang X, de Richter RK, Liu W, Wu T, Pan Y. Numerical analysis on the influence of ambient crosswind on the performance of solar updraft power plant system. *Renew Sust Energ Rev*. 2012;16(8):5567-5583.
52. Fallah SH, Valipour MS. Numerical investigation of a small scale sloped solar chimney power plant. *Renew Energy*. 2022; 183:1-11.
53. Haaf W. Solar chimneys: part ii: preliminary test results from the Manzanares pilot plant. *Int J Sustain Energy*. 1984;2(2): 141-161.
54. Guo P, Li T, Xu B, Xu X, Li J. Questions and current understanding about solar chimney power plant: a review. *Energy Convers Manag*. 2019;182:21-33.
55. Yu HL, Zhang KL, Rossi C. Theoretical study on photocatalytic oxidation of VOCs using nano-TiO2 photocatalyst. *J Photochem Photobiol A*. 2007;188(1):65-73.
56. Li Q, Ouyang Y, Li H, Wang L, Zeng J. Photocatalytic conversion of methane: recent advancements and prospects. *Angew Chem Int Ed Engl*. 2022;61(2):e202108069.
57. Zeng JM, Liu LD, Liang X, Chen SH, Yuan J. Evaluating fuel consumption factor for energy conservation and carbon neutral on an industrial thermal power unit. *Energy*. 2021;232:120887.
58. Muangthai I, Lewis C, Lin SJ. Decoupling effects and decomposition analysis of CO_2 emissions from Thailand's thermal power sector. *Aerosol Air Qual Res*. 2014;14(7):1929-1938.
59. Abdelsalam E, Kafiah F, Alkasrawi M, Al-Hinti I, Azzam A. Economic study of solar chimney power-water distillation plant (SCPWDP). *Energies*. 2020;13(11):2789.
60. Fan QP, Wang X, Li YD. Photo-catalytic activity and life time of the TiO_2 nano-particles. *Chinese J Inorg Chem*. 2003;19(5): 521-526.
61. Wang L, Gong W, Lin A, Hu B. Analysis of photosynthetically active radiation under various sky conditions in Wuhan, Central China. *Int J Biometeorol*. 2014;58(8):1711-1720.

How to cite this article: Ming T, Xiong H, Shi T, et al. A novel green technology: Reducing carbon dioxide and eliminating methane from the atmosphere. *Int J Energy Res*. 2022;1-14. doi:10.1002/er.8675